

Evolution of Self-Assembled Silica–Tetrapropylammonium Nanoparticles at Elevated Temperatures

Jeffrey D. Rimer, Dionisios G. Vlachos,* and Raul F. Lobo*

Center for Catalytic Science and Technology, Department of Chemical Engineering, University of Delaware, Newark, Delaware 19716

Received: April 20, 2005; In Final Form: May 5, 2005

The time evolution of silica nanoparticles in solutions of tetrapropylammonium (TPA) has been studied using a combination of small-angle scattering, conductivity, and pH measurements to provide the first comprehensive analysis of nanoparticle structural and compositional changes at elevated temperatures. We have found that silica–TPA nanoparticles subjected to hydrothermal treatment (70–90 °C) grow via an Ostwald ripening mechanism with growth rates that depend on both pH and temperature. Small-angle X-ray (SAXS) and neutron (SANS) scattering confirm that the core–shell structure of the particles, initially present at room temperature, is maintained during heating, but an evolution toward sphericity is evidenced especially at high values of pH. SAXS absolute intensity calculations were utilized to calculate the changes in nanoparticle composition and concentration over time. These changes along with the conductivity and pH measurements and SANS contrast matching studies indicate that, upon heating, TPA becomes embedded in the core of nanoparticles giving rise to more zeolitic-looking nanomaterials.

Introduction

It has been known that silica in solutions containing tetraalkylammonium (TAA) hydroxide self-assembles to form nanoparticles (2–5 nm in diameter). The observation of nanoparticles both prior to and during the growth of silicalite-1 has generated intense interest concerning their potential role in zeolite growth:^{1–5} most notably of silicalite-1, the purely siliceous form of the well-known zeolite ZSM-5. Two mechanisms for silicalite-1 growth have been proposed: The “nanoparticle addition” mechanism,^{1,6} which assumes nanoparticles directly add to a growing zeolite, and the “monomer addition” mechanism,⁷ which assumes silica dissolves from these nanoparticles in the form of monomers and/or oligomers that then add to the growing zeolite crystal. Despite the numerous studies performed on silicalite-1 growth, the mechanism is still not very well understood. Aside from the scientific interest in the zeolite community, the formation of silica nanoparticles is a phenomenon that extends beyond zeolites to general silicate solutions formed in highly basic solutions of both organic and inorganic cations.⁸ Furthermore, understanding the self-assembly of silica offers the possibility to design novel materials for applications in biomineralization,^{9,10} biomaterials,¹¹ and selective microseparations.¹²

The structure, composition, and morphology of these nanoparticles have been subjects of much debate. Many *ex situ* techniques have been used to study these particles, such as freeze-drying for cryo-transmission electron microscopy (TEM)¹³ or extraction into dry powders for analyses by X-ray diffraction (XRD), infrared (IR) spectroscopy, or atomic force microscopy (AFM).¹⁴ Martens and collaborators have characterized extracted nanoparticles and proposed that the particles have an MFI framework type with a well-defined structure and geometry.^{14–16} On the other hand, recent data on extracted samples of nanoparticles¹⁷ indicated that these particles do not possess the signatures of crystalline zeolite as suggested by Martens and co-workers.

The isolation steps performed in these *ex situ* studies may potentially alter both the structure and morphology of the nanoparticles. *In situ* analyses, such as ²⁹Si NMR, dynamic light scattering (DLS), and small-angle scattering, on the other hand, allow the nanoparticles to be studied noninvasively in their local environment. DLS has been used in the past to analyze the size of the nanoparticles;¹⁸ however, this technique is not reliable for particles with sizes of <10 nm. Small-angle scattering is better suited to determine size and shape in this length scale.

Recent *in situ* studies have generated a clearer picture of the nanoparticle structure and the driving force behind their formation in solution. It has been shown that there exists a critical aggregation concentration (CAC) above which monomeric and/or oligomeric silica in solution self-assembles into nanoparticles.¹⁹ This reversible process occurs in highly basic solutions, resulting in nanoparticle sizes that are independent of the TAA^{19,20} but dependent on the alkalinity of the solution.^{8,21} The particles form core–shell structures with a TAA shell and a silica core that is primarily composed of Q³ species (Qⁿ = SiO_n-(OH)_{4-n}), which differs from the MFI framework of silicalite-1 that is composed mainly of Q⁴ species.^{8,19,22} In addition, the composition of the nanoparticles differs from that of silicalite-1, as evidenced by the lower scattering length density obtained from small-angle neutron scattering (SANS) contrast experiments.^{2,19}

The nanoparticles formed in silicalite-1 solutions have been characterized almost exclusively at room temperature, yet zeolite growth occurs typically at elevated temperatures. In this paper, we use a combination of SANS and small-angle X-ray scattering (SAXS) to examine the evolution of nanoparticles as a function of temperature for two solutions of different alkalinity. Unlike previous analyses,^{21,23,24} the measurements performed here were conducted on dilute silica solutions (volume fraction < 5%) to increase the induction period for silicalite-1 nucleation and eliminate interference

effects, thus allowing direct time-evolution analyses of the nanoparticles.

Experimental Section

Solutions of silica-template nanoparticles were synthesized by first diluting concentrated tetrapropylammonium hydroxide (TPAOH, 40% w/w, Alfa Aesar) in deionized water. After mixing for ~30 min, tetraethyl orthosilicate (TEOS, 98%, Aldrich) was added, and the resulting mixture was vigorously stirred for at least 12 h prior to analysis. To investigate the effects of pH, TPAOH was supplemented by tetrapropylammonium bromide (TPABr, 98%, Aldrich) to lower the hydroxide concentration while maintaining a constant concentration of TPA. Compositions of 40 SiO₂/9x TPAOH/9(1 - x) TPABr/9500 H₂O/160 EtOH were prepared with $x = 1$ (S1 solution) and $x = 0.5$ (S2 solution).

Nanoparticle solutions for SANS experiments were prepared with compositions of 40 SiO₂/9x TPAOD/ 9(1 - x) TPABr/9500 D₂O/160 EtOD using deuterium oxide (Aldrich, 99% D) with $x = 1$ (d-S1 solution) and $x = 0.5$ (d-S2 solution). Background solutions for both d-S1 and d-S2 were prepared with the same composition but without the added TEOS. Solutions for SANS contrast analyses were also prepared with the composition 40 SiO₂/9x TPAOD/9(1 - x) TPAOH/9500x D₂O/9500(1 - x) H₂O/160x EtOD/160(1 - x) EtOH with $x = 1$ (100% D₂O), $x = 0.7$ (70% D₂O), $x = 0.5$ (50% D₂O), $x = 0.3$ (30% D₂O), and $x = 0$ (0% D₂O). The TPAOD used in all solutions was synthesized from a mixture of 5 TPABr/5 AgO/610 D₂O using silver oxide (Aldrich). The solution was covered to prevent exposure to visible light, stirred for 4 days, and then filtered. The conversion of TPABr to TPAOD was measured by titration with HCl_(aq) to be 78%, resulting in a 0.34 M TPAOD solution containing 0.097 M excess TPABr. Thus, d-S1 solutions contain a small amount of TPABr (~0.01 M).

To investigate the nanoparticle evolution at higher temperatures, the solutions were first filtered with a 0.45- μ m membrane (Pall Corp.). The samples were placed in sealed, 15-mL polypropylene centrifuge tubes, which were submerged in a water bath regulated at 70–90 °C. Equilibrium temperature was reached within 5 min of heating, and the individual samples were removed at various times and quenched to room temperature prior to analysis. The conductivity measurements were obtained with a VWR model 2052 EC meter, and the pH was measured using a Corning 355 pH/ion analyzer and a Corning high-performance electrode with Ag-ion barrier. The pH meter was calibrated with standardized pH 10 and 12 buffer solutions (Alfa Aesar).

SAXS experiments were conducted on a SAXSess (Anton-Paar) system. Samples were placed in a vacuum-tight 1-mm-diameter quartz capillary holder and measured at 25 °C. A monochromatic, line-collimation source of CuK α radiation ($\lambda = 1.54$ Å) was used with a 265-mm sample-to-detector distance. The scattering patterns were collected over a 20-min period on a phosphor imaging plate within the q range 0.1–8 nm⁻¹. Patterns were normalized to the height of the primary beam signal using the SAXSquant software. Desmearing was conducted by subtracting the signal from a normalized background sample.

SANS experiments were carried out using the 30-m diffractometer (NG3) at the National Institute of Standards and Technology (NIST) in Gaithersburg, MD. Samples were filtered (0.45- μ m membrane) and placed in quartz cells of 4-mm path length. A constant neutron wavelength of 6 Å was used with two sample-to-detector distances (13.0 and 2.0 m) to provide a

q range of 0.6–3 nm⁻¹. Longer distances were run for 50 min to capture the low q values, while the shorter distances were run for 30 min. The software provided by NIST was used for the normalization of the data, and the subtraction of the sample holder and desmearing was conducted through background subtraction.

Data Analysis Methods

Guinier Analysis. Prior to fitting the SAXS and SANS patterns, the Guinier region was analyzed to identify the lowest q value at which the structure factor is negligible. The Guinier region is defined as $qR_L < 1$, where R_L is the characteristic length of a particle and q is the scattering vector, which is given by

$$q = \frac{4\pi}{\lambda} \sin \theta \quad (1)$$

A plot of $\ln[I(q)q^x]$ versus q^2 (I denotes intensity) generates a straight line for the scattering from spheres ($x = 0$), cylinders ($x = 1$), and plates ($x = 2$).²⁵ Interference effects arising from particle interactions cause deviations in the Guinier plot. Thus, the low q limit can be identified, and q values below this limit are excluded from form-factor analyses of small-angle scattering patterns.

Pair Distance Distribution Function. The pair distance distribution function (PDDF) was generated from the scattering patterns using the indirect Fourier transform (IFT) method developed by Glatter.^{26,27} The IFT method represents the PDDF, $P(R)$, as a linear combination of functions $\varphi_i(R)$

$$P(R) = \sum_{i=1}^N a_i \varphi_i(R) \quad (2)$$

where $\varphi_i(R)$ are cubic β -splines and a_i are weighting factors determined by least-squares fits of the scattering data. The intensity and distance distribution are related through a Fourier transform

$$I(q) = 4\pi \int_0^\infty P(R) \frac{\sin(qR)}{qR} dR \quad (3)$$

The IFT method is applicable to dilute particle systems (<5 vol %) and provides a model-independent way of obtaining the PDDF.²⁸ The technique can be extended to systems where the structure factor is substantial using the generalized indirect Fourier transform (GIFT) method, which requires a priori knowledge of the nature of interparticle forces to select an appropriate structure factor model.

Modeling Small-Angle Scattering Data. Small-angle scattering patterns were fit with the software developed by NIST to obtain information on particle size and shape.²⁹ The scattering intensity is fitted with a form factor, $P(q)$, and a structure factor, $S(q)$, through the relationship

$$I(q) = v_i(\text{contrast})^2 VP(q) S(q) \quad (4)$$

where v_i is the volume fraction, V is the particle volume, and “contrast” is the difference in scattering length density (SLD) between the particle and the solvent. Analytical functions for the form factor were used to fit the scattering patterns as monodisperse uniform ellipsoids,³⁰ cylinders, spheres, and core-shell particles.³¹ The Hayter–Penfold mean spherical approximation (HPMSA) structure factor was used to account for the effect of interparticle forces due to the coulomb repulsion

between charged particles (these are not expected to be large because of the high dilution of our solutions and the relatively high ionic strength of 0.05–0.10 M).

The model fitting parameters are volume fraction, background, surface charge, and particle dimensions. The input parameters include temperature (298 K), dielectric constant, ionic strength, and contrast, all of which are held constant. The ionic strength for S1 and S2 solutions are 0.054 and 0.081 M, respectively. The dielectric constant, calculated using the Clausius–Mosotti relation,³² is 70.31 for a 160 EtOH/9500 H₂O solution. The contrast values for SAXS and SANS solutions were obtained using the SLDs, reported in Table S1 (see Supporting Information).

Contrast Variation Analyses in SANS. The scattering intensity, $I(q)$, from particles suspended in solution depends on the contrast, or difference in SLD between the solid and the solvent. Isotope substitution in SANS offers the capability of drastically changing the contrast: a technique which can be used to identify an unknown particle SLD. To achieve a wide range of contrast, the hydrogen-to-deuterium ratio in the solution is varied. For the solutions studied in this paper, only the solvent SLD is changed using a combination of D₂O and H₂O. At the composition where $SLD_{\text{solvent}} = SLD_{\text{solid}}$, the scattering intensity becomes zero, and this point is referred to as the *match point*. To identify the match point, the parameter $I(0)_{\Delta}$, which is the difference in intensity at the high ($q \approx 3 \text{ nm}^{-1}$) and low ($q \approx 0.2 \text{ nm}^{-1}$) q values of the SANS pattern, is calculated. Plotting $I(0)_{\Delta}^{1/2}$ versus mol % D₂O results in a pseudo-quadratic function that has a minimum, where $I(0)_{\Delta}^{1/2}$ values on one side of the minimum are assigned negative values and linear regression is used to identify the match point (i.e., % D₂O at which $I(0)_{\Delta}^{1/2} = 0$).²

Extracting Absolute Intensities From SAXS. The raw intensities measured by SAXS are typically given in arbitrary units. These can be converted into an absolute scale by calculating the differential scattering cross-section per unit volume²⁵

$$\left(\frac{d\Sigma}{d\Omega}\right)(q)(\text{cm}^{-1}) = \frac{I_{\text{S+SB}}^m - I_{\text{SB}}^m \cdot A_3}{I_{\text{H}_2\text{O+ec}}^m - I_{\text{ec}}^m \cdot A_4} \quad (5)$$

where the intensities, I , are scaled by their respective transmissions and the symbols S, SB, and ec represent sample, sample background, and empty cell, respectively. The constant A_3/A_4 is the scattering intensity of water, which is a function of the water compressibility and has a value of 0.01632 cm^{-1} at 293 K.³³ The quantity $I_{\text{H}_2\text{O+ec}}^m - I_{\text{ec}}^m$ is a constant with an average value measured between $1 < q < 4 \text{ (nm}^{-1}\text{)}$ according to the procedure used by Glatter and co-workers.³³

The concentration of particles can be obtained from the absolute intensity using the following expression for which we assume no particle interactions (i.e., $S(q) = 1$)^{25,33}

$$\frac{d\Sigma}{d\Omega}(q, c) = c \cdot K \cdot M \cdot P(q) \quad (6)$$

where c is the mass concentration of particles, M is the (apparent) molecular mass, and K is the scattering constant ($\text{cm}^2 \text{ mol g}^{-2}$) given by

$$K = (\text{contrast})^2 v^2 / (M^2 N_A) \quad (7)$$

where v is the partial molar volume. The molecular mass is calculated as $M = V\rho N_A$, where V is the particle volume, ρ is the particle density (g/cm^3), and N_A is the Avogadro number.

The contrast is expressed as the difference in SLD between the nanoparticle, which is a linear combination of both water and silica, and the background solution

$$\text{contrast} = [x_{\text{SiO}_2} \text{SLD}_{\text{SiO}_2} + (1 - x_{\text{SiO}_2}) \text{SLD}_{\text{H}_2\text{O}}]_{\text{nanoparticle}} - \text{SLD}_{\text{background}} \quad (8)$$

where x_{SiO_2} is the molar fraction of silica, and the SLD for silica and water are 1.89×10^{-5} and $9.46 \times 10^{-6} \text{ \AA}^{-2}$ ($\text{CuK}\alpha$, $\lambda = 1.54 \text{ \AA}$), respectively.

Equation 6 is evaluated at $q = 0 \text{ nm}^{-1}$ where $P(0) = 1$, and $d\Sigma/d\Omega(0, c)$ is obtained through linear extrapolation of a Guinier plot. The density and the contrast of the nanoparticle are unknown. The nanoparticle core is composed of hydrated silica in which the particle density is expressed as

$$\rho = m_{\text{SiO}_2} \rho_{\text{SiO}_2} + (1 - m_{\text{SiO}_2}) \rho_{\text{H}_2\text{O}} \quad (9)$$

where m_i is the mass fraction of species i , and the densities, ρ_i , of silica (amorphous) and water are taken as 2.2 and 1.0 g/cm^3 , respectively.

In solution, equilibrium exists between silica in the form of solid nanoparticles and as monomers and/or oligomers. The amount of dissolved silica in solution depends on the solubility of silica. For simplicity, we consider all dissolved silica to be in the form of monomers. We can then express the total silica concentration in solution as

$$[\text{SiO}_2]_{\text{total}} = [\text{SiO}_2]_{\text{monomer}} + [\text{SiO}_2]_{\text{nanoparticle}} \quad (10)$$

The monomer concentration can be approximated as the CAC, which is the silica concentration above which nanoparticles begin to self-assemble. The CAC represents the solubility limit of monomer in solution. Fedeyko et al. approximated the CAC as a function of pH with the following linear relationship¹⁹

$$[\text{SiO}_2]_{\text{CAC}} = 24.147 \cdot [\text{OH}^-] + 0.016 \quad (11)$$

The molar concentration of silica in the nanoparticles is related to the silica mass fraction and the mass concentration of particles using

$$[\text{SiO}_2]_{\text{nanoparticle}} = \frac{m_{\text{SiO}_2} \cdot c}{M_{\text{SiO}_2}} \quad (12)$$

where the molecular weight of silica M_{SiO_2} is 60 g/mol . Substituting eqs 11 and 12 into 10, the mass fraction of silica is determined and is used to calculate the particle density from eq 9, the number of silicon atoms per particle ($M m_{\text{SiO}_2} / M_{\text{SiO}_2}$), and the number density ($n_p = c N_A / M$).

Results and Discussion

pH and Conductivity Evolution at Higher Temperatures.

The conductivity and pH were measured for S1 and S2 solutions heated at $70\text{--}90 \text{ }^\circ\text{C}$ over a 6-h period. It is observed that both the pH and the conductivity of the solutions increase with time. Figure 1 shows the measurements for the S1 solution heated at $70 \text{ }^\circ\text{C}$. There is a sharp increase in both the pH and the conductivity within the first hour of heating followed by a leveling of the curves as time progresses. S1 solutions heated for 18 h show that the pH and the conductivity do not reach equilibrium, but continue to increase at a slow rate. In addition, when the heated nanoparticle solutions are stored for months at room temperature, no substantial change in the pH and the

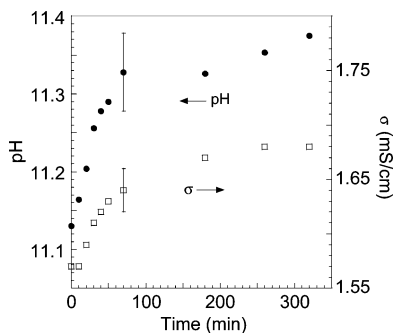


Figure 1. Conductivity, σ , and pH measurements of an S1 solution heated at 70 °C over a 320-min period. The conductivity was obtained from conductivity meter readings with an accuracy of ± 0.02 mS/cm, and the pH is measured by a pH electrode with an accuracy of ± 0.05 . The error bars are two standard deviations obtained from four experiments.

TABLE 1: Net Increase in the Hydroxide Concentration and Conductivity for Heated S1 and S2 Solutions, as Measured between the Initial ($t = 0$ min) and Final ($t = 320$ min) Times

T (°C)	S1 solution		S2 solution	
	$\Delta[\text{OH}^-]$ $\times 10^4$ M	$\Delta\sigma$ (mS/cm)	$\Delta[\text{OH}^-]$ $\times 10^4$ M	$\Delta\sigma$ (mS/cm)
70	5.2	0.11	1.7	0.10
80	7.8	0.20	2.8	0.12
90	9.8	0.22	3.1	0.15

conductivity is observed. Thus, the change in solution composition resulting from heat treatment appears as an irreversible process over the time scales examined, presumably due to large kinetic barriers involved in this process, or most probably because nanoparticles formed at room temperature correspond only to a local minimum of free energy of the system.

The results for the net change in $[\text{OH}^-]$ and conductivity, σ , for both sets of solutions are listed in Table 1. At room temperature, the S1 and S2 solutions have pH values of ~ 11.2 and 10.2, respectively.

Heating the solutions results in changes, $\Delta[\text{OH}^-]$ and $\Delta\sigma$, that increase with increasing temperature and solution alkalinity. Thus, the S1 solution exhibits larger net increases than the lower alkaline S2 solution.

The time evolution of pH during the synthesis of silicalite-1 has also been studied by Cundy et al. and Yang and Navrotsky.^{4,34} Both report that for highly basic solutions ($\text{pH} > 12$), the pH is constant for much of the silicalite-1 growth; however, during the initial stage of heating, there is no reported change in the solution pH. In this paper, much lower TPAOH/ H_2O ratios have been used. From Table 1, it is observed that $\Delta[\text{OH}^-]$ increases with solution alkalinity, which would suggest that as the pH of the solution approaches values above 12, $\Delta[\text{OH}^-]$ continues to increase. Because of the logarithmic relationship between pH and $[\text{OH}^-]$, the ΔpH measured experimentally for solutions with $\text{pH} > 12$ would be expected to be within the error of the pH meter reading (± 0.05). Thus, it may be possible that the solutions studied in refs 4 and 34 also show similar behavior to those reported here, but they are not measurable using a pH meter.

To test the above hypothesis, we prepared a solution of composition 25 $\text{SiO}_2/9$ TPAOH/480 $\text{H}_2\text{O}/100$ EtOH (according to ref 4). The pH and the conductivity of the solution at room temperature were 12.68 and 4.24 mS/cm, respectively. After heating the solution for 6 h at 90 °C, the ΔpH and $\Delta\sigma$ were measured to be 0.04 ± 0.05 and 0.71 ± 0.02 mS/cm, re-

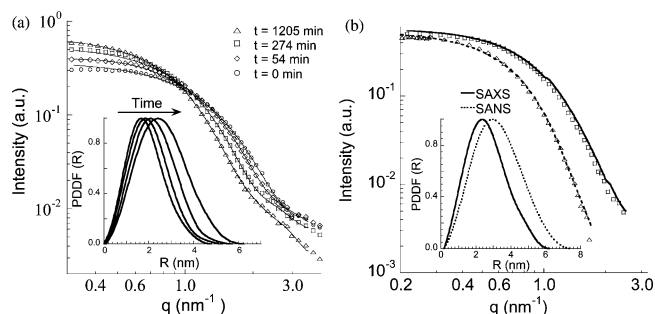


Figure 2. Small-angle scattering analyses illustrating the nanoparticle evolution at 70 °C. (a) SAXS patterns and corresponding PDDFs (inset) of the S1 solution taken at various times. (b) Comparison of SAXS (squares) and SANS (triangles) patterns and corresponding PDDFs (inset) for the d-S1 solution heated for 7 h. In the intensity curves, the symbols represent the experimental data, and the lines are IFT fits.

spectively. Therefore, the change in pH is very small and within experimental error, which explains why previous studies have not reported an initial increase in alkalinity. The net increase in conductivity is in agreement with the trends shown in Table 1 (i.e., an increase in conductivity with higher alkalinity) as is $\Delta[\text{OH}^-]$, which has a value of 4.6×10^{-3} M, and hence, the particles in refs 4 and 34 should also change as they are heated.

Evolution of Nanoparticle Size and Shape Upon Heating. Small-angle scattering was used to monitor the changes of an S1 solution at elevated temperatures (Figure 2a). As time progresses, the intensities of the SAXS patterns increase, and the peak maxima shift to lower q values. The corresponding PDDFs for each pattern were calculated using IFT analysis and are shown in the inset of Figure 2a. There is a clear increase in particle size as both the peak maximum and the width of the PDDF shift to higher R values with increasing time (where R stands for the distance between atoms). The general shape of the PDDF reflects the morphology of the nanoparticle, which for monodisperse nanoparticles has been shown to be consistent with an ellipsoidal shape at room temperature.¹⁹ Visual inspection indicates that the ellipsoidal shape is maintained for the heated nanoparticles during the evolution (see below).

To test whether the core-shell structure is maintained for the nanoparticles at higher temperatures, a d-S1 solution was heated and analyzed with both SAXS and SANS. Simultaneous use of these two scattering techniques allows a core-shell structure to be revealed on the basis of the differences between neutron and X-ray interactions with atoms. In particular, X-rays scatter from the electron cloud of an atom, whereas neutrons scatter from the atom's nucleus. Thus, X-rays exhibit large scattering intensities from silicon atoms but not from TPA molecules ($\lambda = 1.54$ Å; $\text{SLD} = 9.6 \times 10^{-6}$ Å⁻²), which have a similar SLD to that of water. Neutrons, on the other hand, scatter strongly from TPA molecules ($\lambda = 6$ Å; $\text{SLD} = -0.49 \times 10^{-6}$ Å⁻²), and thus, they can detect the presence of a TPA shell surrounding the silica nanoparticle. Figure 2b shows the SAXS and SANS data of a d-S1 solution heated at 70 °C for 7 h. On the basis of the PDDF, nanoparticles observed using SANS are larger than those seen using SAXS. By comparing the differences between the widths of the two PDDF plots, the thickness of the shell is 0.9 ± 0.3 nm, which is approximately the size of a TPA molecule. Thus, high-temperature nanoparticles retain the core-shell structure of low-temperature nanoparticles. This conclusion has been reached over the entire temperature and time ranges studied here.

The scattering patterns were fit with a form factor and a structure factor to estimate the change in size and shape of the evolving nanoparticles using eq 4 and the software provided

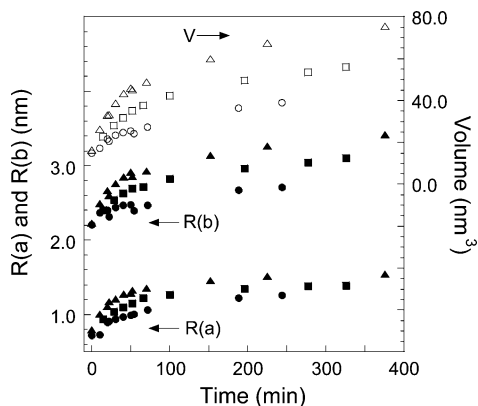


Figure 3. Plots of the $R(a)$ and $R(b)$ values obtained from the ellipsoid fits with corresponding volumes to SAXS patterns of S1 solutions heated at 70 °C (circles), 80 °C (squares), and 90 °C (triangles).

by NIST.²⁹ The shape of the nanoparticle was determined by choosing a model that best fits the SAXS intensities from S1 solutions heated for various times and temperatures with varying geometrical form factors, namely, a sphere, a uniform ellipsoid, a cylinder, and a core–shell ellipsoid. It was found that the relative goodness of the model fit is independent of the temperature and the duration of heating. Figure S1 in the Supporting Information compares the fits of three models to the same SAXS pattern. The uniform ellipsoid model provides the best overall fit with monodisperse nanoparticles, which agrees with IFT analysis and previously reported results of room-temperature samples.¹⁹ Thus, the uniform ellipsoid form factor with the HPMSA structure factor was used to fit all small-angle scattering patterns in this paper. The core–shell model (not shown) also provides relatively good fits of the SANS data, but comparisons of the core dimensions to uniform model fits of the SAXS patterns are inconsistent. Possible reasons for this may include inaccurate SLDs for the core and the shell, as well as the possibility of TPA inclusion in the growing core upon heating, an issue that is further discussed below.

Analyses of SAXS data from S1 solutions were performed by heating the solutions for various times at 70, 80, and 90 °C. Figure 3 shows the radii $R(a)$ and $R(b)$ values from the ellipsoid model fits along with the corresponding volume, which is given by

$$V_{\text{ellipsoid}} = \frac{4}{3} \pi R(a)R(b)^2 \quad (13)$$

The nanoparticles have an oblate spheroid, or disklike, shape (i.e., $R(b) > R(a)$) that increases in size with time upon heating. The effective charge calculated from the HPMSA structure factor for all fits is approximately zero, indicating that interparticle forces are negligible, which was verified by obtaining equally good fits without the inclusion of a structure factor.

The evolution experiments are not formally *in situ*, as the samples are cooled to room temperature. However, we have found that the particle structure becomes more stable as they evolve over time at higher temperatures, and consequently, structural changes are not expected from cooling the samples.

Experiments over an 18-h period of heating show that the particles continue to grow. Figure 3 indicates that the evolution is an activated process, and the final nanoparticle size is dependent on both the temperature and the duration of heating. The particle aspect ratio, $R(a)/R(b)$, as shown in Figure 4, increases with time, that is, particles become slightly more spherical.

In passing, we should comment about the possibility of polydispersity. Recent work by Fedeyko et al. has shown that

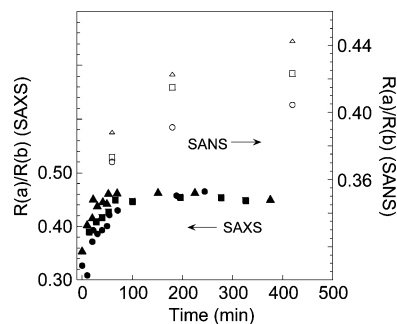


Figure 4. Comparison of the aspect ratios, $R(a)/R(b)$, obtained from ellipsoid fits to the S1 (SAXS) and d-S1 (SANS) solutions at 70 °C (circles), 80 °C (squares), and 90 °C (triangles).

SANS data of room-temperature S1 particles can be fit with core–shell models employing both ellipsoid and polydisperse sphere form factors.⁸ The polydispersity, P , is given by

$$P = \frac{\sigma_R}{R_{\text{ave}}} \quad (14)$$

where R_{ave} is the average radius and σ_R is the root-mean-square deviation. The polydispersity of nanoparticles at 25 °C is low (~ 0.2). The same analysis is performed here with the heated S1 samples to determine how the polydispersity changes over the course of the evolution. The PDDF of the SAXS patterns for samples heated at 70, 80, and 90 °C were fit by summing the analytical PDDF curves for a Gaussian distribution of spheres,³⁵ in which the parameters R_{ave} and σ_R were obtained by minimizing the distance from the experimental PDDF using *Matlab* (details of the fits and fitting procedure are provided in Figure S2 of the Supporting Information). Over the temperature and time ranges studied, the polydispersity remains relatively constant, but in some cases shows a slight decrease over time. Thus, from the results, we expect a variation of ± 0.3 nm in the particle radius due to polydispersity, a number that is entirely conceivable. This variation is similar to the uncertainty estimated for monodisperse model fits (± 0.1 nm). At this stage, a polydisperse model cannot unambiguously be ruled out because of the accuracy of such measurements. In fact, the mechanism of nanoparticle evolution upon heating discussed below corroborates the existence of some polydispersity. Since the sizes inferred from the monodisperse and polydisperse models are comparable, for the remaining of the paper, the nanoparticles are assumed to be monodisperse.

Mechanism for Nanoparticle Evolution. The absolute intensities from SAXS patterns of an S1 solution heated at 70 °C were obtained using eq 5 (See Methods section). The results in Figure 5 show that the number density of nanoparticles decreases with time while the number of silicon atoms per particle increases. Another interesting inference comes from the pH and conductivity changes in solution shown in Figure 1. The monomer concentration is estimated as the CAC, given by eq 11, which is the solubility limit of silica in solution. Given the fact that the pH increases with time, the concentration of silica monomers increases during nanoparticle evolution, as shown in Figure 5. Therefore, we infer that silica from the dissolving particles serves to supply monomer to solution and growth units to the growing nanoparticles.

The aforementioned observations point to the evolution of nanoparticles being described by an Ostwald ripening process whereby a fraction of the initial nanoparticle population grows at the expense of the rest that dissolve over time.

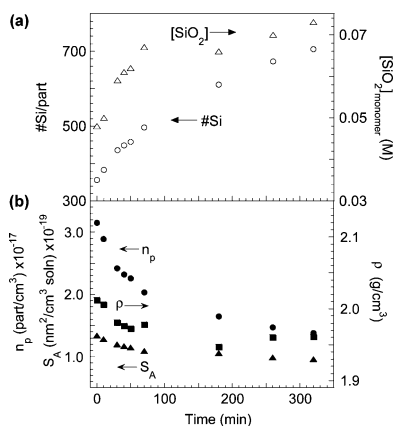


Figure 5. Compositional changes to an S1 solution heated at 70 °C over a 320-min period. (a) Plots of the number of silicon atoms per particle and the silica monomer concentration, using eq 11. (b) Plots of the number density, n_p , particle density, ρ , and the total surface area of particle cores per volume of solution, S_A .

To quantitatively assess the idea of a nanoparticle aggregation mechanism, a simple dimerization kinetic model in which spherical primary particles, A_1 , coalesce to form dimers, A_2 , has been considered according to



In this model, the rate-determining step is taken as the rate of successful collision, and particle shape reorganization is considered to be relatively fast. The instantaneous concentrations of primary particles, C_1 , and dimers, C_2 , are given by

$$\frac{dC_1}{dt} = -2kC_1^2 \quad (16)$$

$$\frac{dC_2}{dt} = kC_1^2 \quad (17)$$

The scattering intensity for a solution of primary particles and dimers is calculated by summing the contributions from each population of particles using

$$I(q, r) = (\text{contrast})^2 N_A [C_1 V_1^2 P_1(q, r_1) + C_2 V_2^2 P_2(q, r_2)] \quad (18)$$

where V_i is the particle volume, $P_i(q, r_i)$ is the form factor, r_1 is the primary particle radius, and r_2 is the dimer radius, which is taken as $\sqrt[3]{2}r_1$. The form factor for a sphere has a simple analytical expression²⁸

$$P_i(q, r_i) = \left\{ \frac{3[\sin(qr_i) - qr_i \cos(qr_i)]}{(qr_i)^3} \right\}^2 \quad (19)$$

The primary particle radius and initial concentration were obtained from the absolute intensity calculations and taken as 1.75 nm and 5.2×10^{-4} M, respectively. The reaction constant ($k = 0.13 \text{ mol L}^{-1} \text{ s}^{-1}$) was chosen to minimize the residual between the experimental intensity and the dimerization model intensity from eq 18 (fits are shown in Figure S3 of the Supporting Information).

The resulting intensity was fit with a monodisperse sphere model to obtain the average particle radius, R_{ave}

$$I(q, r) = (\text{contrast})^2 N_A (C_1 + C_2) V(R_{\text{ave}})^2 P(q, R_{\text{ave}}) \quad (20)$$

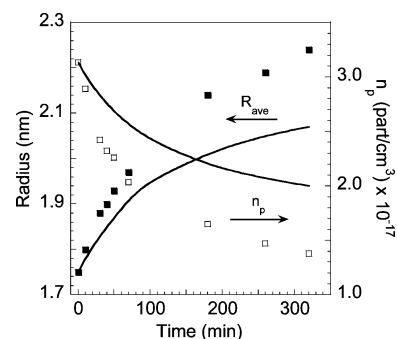


Figure 6. Comparison of the dimerization model results (lines) to SAXS data (symbols) of S1 particles heated at 70 °C. The number density of both primary particles and dimers, $n_p = N_A(C_1 + C_2)$, and their average radii were obtained using a reaction constant $k = 0.13 \text{ mol L}^{-1} \text{ s}^{-1}$.

Figure 6 compares the results of the dimerization model to the SAXS absolute intensity calculations. The average radius and the total number density, $n_p = N_A(C_1 + C_2)$, from the dimerization model are plotted alongside the experimental values obtained using a uniform spherical particle. The dimerization model cannot simultaneously capture the trends in $I(q, r)$, R_{ave} , and n_p . Thus, given these differences, it is unlikely that the nanoparticle growth observed in Figures 2 and 3 is associated with particle coalescence. In addition, the small increment in particle size increase and the rise in monomer concentration shown in Figure 5 exclude the possibility of larger aggregates (trimers, etc.) forming during the course of the evolution.

Changes in Nanoparticle Composition Upon Heating. The SAXS absolute intensity analyses reported for the S1 solution heated at 70 °C are considered here to estimate changes in composition of nanoparticles upon heating. An uncertainty analysis was performed on the absolute intensity calculations (specifically, the uncertainty in n_p , m_{SiO_2} , and contrast was computed) to determine the variation expected from errors in experimental measurements (see Table S2 in Supporting Information) and the effect of particle shape and polydispersity (Figure S4 in Supporting Information).

The results in Figure 5 show that there is a 30% reduction in the total surface area of the nanoparticle cores over time (this value is independent of the shape model used; see Figure S4 in Supporting Information). The approximate area occupied by a single TPA molecule, $S_{A, \text{TPA}}$, is 0.81 nm² (based on values reported by Claesson et al.³⁶). The coverage of TPA on the nanoparticle surface is unknown, but an upper bound can be estimated by assuming that the TPA molecules are closely packed in a uniform monolayer on the surface. The TPA loss from the nanoparticle surface, $[\text{TPA}]_{\text{surface}}$, due to the surface area reduction is given by

$$\Delta[\text{TPA}]_{\text{surface}} = \frac{S_{A,t} - S_{A,t=0\text{min}}}{S_{A, \text{TPA}}} \quad (21)$$

Thus, on the basis of surface area reduction resulting from heating, a maximum of $45 \pm 6 \times 10^{17}$ TPA/cm³ are either incorporated into the growing particle core or displaced into the bulk solution.

During evolution, the particle mass density decreases with time as shown in Figure 5, indicating that the nanoparticles at elevated temperatures become more hydrated or TPA gets included in the core. The latter scenario can be envisioned by silica condensing around the adsorbed TPA on the particle surface, thus embedding the initial template adsorbed at room temperature into the growing core. Given that TPAOH has a

density of 0.98 g/cm³, which is nearly equal to that of water, the nanoparticle core density given in eq 9 can be rewritten at high temperatures as

$$\rho \approx m_{\text{SiO}_2} \rho_{\text{SiO}_2} + (m_{\text{H}_2\text{O}} + m_{\text{TPA}}) \rho_{\text{H}_2\text{O}} \quad (22)$$

Assuming that the net density change in Figure 5 is purely associated with TPA inclusion, the maximum amount of TPA that can become embedded in the nanoparticle cores, [TPA]_{density}, over a 320-min period is $48 \pm 6 \times 10^{17}$ TPA/cm³.

$$\Delta[\text{TPA}]_{\text{density}} = \left(\frac{m_{\text{H}_2\text{O}} \rho V N_A n_p}{M_{\text{WTPA}}} \right)_t - \left(\frac{m_{\text{H}_2\text{O}} \rho V N_A n_p}{M_{\text{WTPA}}} \right)_{t=0\text{min}} \quad (23)$$

This results in ~ 35 TPA molecules per nanoparticle core, which is reasonable considering that a Si-ZSM-5 molecule of the same volume contains 33 TPA.³⁷ Therefore, comparison of surface area and density calculations indicates that TPA inclusion is a clear possibility. To obtain more definitive evidence, we turn to conductivity measurements.

The conductivity of the solution is calculated using a variation of the Shedlovsky equation³⁸

$$\sigma = \sum \lambda_i C_i - \sum (A + B \lambda_i) C_i^{3/2} + \sum D \cdot C_i^a \quad (24)$$

where C_i is the concentration of a charged ion or molecule and λ_i is the corresponding limiting molar conductivity. The Debye–Hückel–Onsager coefficients, A and B , were obtained from literature for an aqueous solution ($A = 60.2$ (mS/cm)(mol/L)^{-1.5}, $B = 0.23$ (mol/L)^{-0.5}).³⁹ The empirical constants D (14.5 (mS/cm)(mol/L)^{-1.2}) and a (1.2) are the average values obtained from conductivity fits for solutions of TPABr, TPAOH, and TPAOH in water (see Figure S5 of the Supporting Information). The ionic species in the S1 solution that contribute to the conductivity are OH⁻, TPA⁺, and charged silica species. Since the presence of various oligomeric species makes the determination of λ_i for silica difficult, only the changes in OH⁻ and TPA⁺, which have reported limiting molar conductivities of 198.3 and 23.42 S cm² mol⁻¹, respectively,⁴⁰ will be considered for the following analysis.

The change in conductivity measured experimentally, shown in Figure 1, is 0.11 ± 0.02 mS/cm. With eq 24, the increase in conductivity from changes in pH, $\Delta\sigma_{\text{OH}}$, is 0.20 ± 0.04 mS/cm and is larger than the measured one, suggesting that TPA is removed from solution. Since the surface area is reduced, this implies that TPA gets embedded into the nanoparticles. Figure 7 shows the comparison between experimental and predicted conductivity changes in the solution. The predicted conductivities take into account the change in pH and the TPA in solution. Two cases are considered: the reduction of TPA on the surface due to surface area reduction ([TPA]_{surface}) that is all released into solution and the net change of TPA in solution that accounts for the surface area reduction and the density changes of the core, ($\Delta[\text{TPA}]_{\text{net}} = \Delta[\text{TPA}]_{\text{surface}} + \Delta[\text{TPA}]_{\text{density}}$). For the latter term, we have assumed all changes in density are associated with TPA inclusion ($48 \pm 6 \times 10^{17}$ TPA/cm³), which gives an upper estimate for the comparison. From Figure 7, we see that a release of TPA into the solution results in a $\Delta\sigma$ that is 3 times the observed value. The simultaneous inclusion of TPA into the particle, on the other hand, results in $\Delta\sigma$ values that are much closer to the experimental observation. Therefore, the conductivity analysis provides the strongest evidence that during

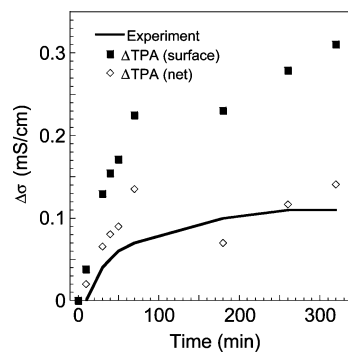


Figure 7. Comparison of the change in conductivity, $\Delta\sigma$, measured experimentally to the predicted values using eq 24 for the changes in pH, TPA released into solution from the nanoparticle surface ($\Delta[\text{TPA}]_{\text{surface}}$), and the TPA incorporated into the nanoparticle core ($\Delta[\text{TPA}]_{\text{net}}$).

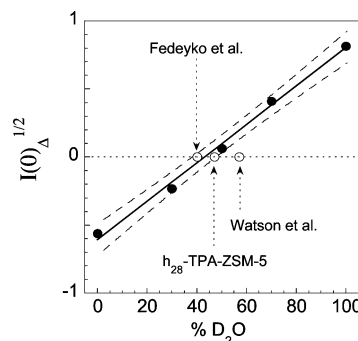


Figure 8. Contrast variation plot for the S1 solution heated at 90 °C for 7 h. The experimental contrast points (solid symbols) were analyzed with linear regression (solid line) to obtain a match point of 43% D₂O for the evolved nanoparticles. The dashed lines are the 95% confidence intervals from the regression analysis. The open symbols represent the match points reported in contrast variation analyses by Fedeyko et al. (40%)¹⁹ and Watson et al. (59%)⁴¹ along with the expected match point for silicalite-1, or h₂₈-TPA-ZSM-5 (47%)⁴¹.

heating TPA gets incorporated within the nanoparticle in addition to maintaining a shell of TPA.

The above analyses were performed with the assumption of a monolayer of TPA; however, the experimental conductivity measurements can also be explained by assuming the nanoparticles at $t = 0$ min have a sub-monolayer coverage ($\sim 35\%$) of TPA, and over the course of evolution, the monolayer coverage increases to 100%. Without knowledge of the nanoparticle surface, it is difficult to distinguish whether TPA becomes embedded in the particle core or the TPA coverage changes over time. Presently, we can only state that the number of TPA molecules per nanoparticle increases over time and that density analyses, along with the contrast variation results presented below, lend strong evidence to the incorporation of TPA into the core.

Contrast Variation Analysis. A contrast variation study was performed on an S1 solution to analyze the SLD of evolved nanoparticles. Five solutions were prepared of the composition $40 \text{ SiO}_2/9x \text{ TPAOD}/9(1-x) \text{ TPAOH}/9500x \text{ D}_2\text{O}/9500(1-x) \text{ H}_2\text{O}/160x \text{ EtOD}/160(1-x) \text{ EtOH}$ with $x = 0, 0.3, 0.5, 0.7,$ and 1.0. The solutions were heated at 90 °C for 7 h prior to SANS analysis. Figure 8 shows the contrast variation plot with the linear regression fit and corresponding 95% confidence intervals.

The match point for the evolved nanoparticles occurs at 43% D₂O, which has a corresponding nanoparticle SLD of $2.44 \times 10^{-6} \text{ \AA}^{-2}$ ($\lambda = 6.0 \text{ \AA}$). Previous contrast studies of a room-temperature S1 solution resulted in a match point at 40% D₂O.¹⁹

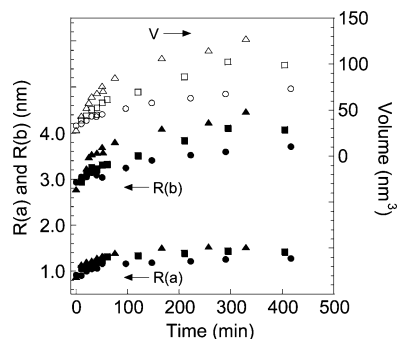


Figure 9. Plots of the $R(a)$ and $R(b)$ values obtained from the ellipsoid fits to the SAXS patterns with corresponding volumes for the S2 solution heated at 70 °C (circles), 80 °C (squares), and 90 °C (triangles).

Therefore, the SLD of the evolved nanoparticles is slightly higher than that of the room-temperature sample.

Watson et al. performed contrast variation analysis of a solution with the composition 8.33 SiO₂/2.47 Na₂O/1.0 TPABr/1000 H₂O that was heated at 100 °C for 5 h.² They reported a match point of 57 mol % D₂O, which is significantly higher than the value obtained from the S1 solution. There are two distinct differences between the particles analyzed in this paper and those reported by Watson et al. In their case, they used sodium silicate solutions, which could potentially lead to particles of different density than those formed from TEOS solutions. Second, the nanoparticle solutions prepared by Watson et al. have much higher alkalinity, which may affect the connectivity and/or the hydration of silica in the particle core.

The match points for colloidal silica and silicalite-1 (h₂₈-TPA-Si-ZSM-5) have been reported as 59 and 47 mol % D₂O, respectively.² Figure 8 indicates that heating the nanoparticles slightly increases the match point, which would indicate a shift in particle composition toward that of silicalite-1. The match points for room-temperature nanoparticles and silicalite-1 both fall within the 95% confidence intervals of the evolved nanoparticles. Thus, while a shift in the particle SLD toward that of silicalite-1 is found, the contrast variation study cannot precisely determine the nanoparticle composition. The increase in the match point upon heating, though, is consistent with the analysis above indicating that the TPA/Si ratio in the nanoparticle is increasing upon heating.

Effects of pH on Nanoparticle Evolution. The effect of pH on nanoparticle evolution was studied by analyzing an S2 solution (pH ≈ 10.2) and comparing it to the S1 solution (pH ≈ 11.1). Figure 9 shows the dimensions obtained from heated S2 solutions along with the corresponding oblate ellipsoid volumes. The nanoparticle size is dependent on pH;^{8,19} thus, the initial size of the S2 particle is larger than those formed in the S1 solutions. The S2 particles maintain a core-shell structure (see Figure S6 of the Supporting Information), and over the range of temperature, pH, and times studied, the core-shell thickness remains relatively unchanged for both S1 and S2 particles (Table S3 in Supporting Information).

Table 2 lists the net change in $R(a)$ and $R(b)$ for both solutions as a function of temperature. The S2 solution exhibits larger growth along the b axis, while the change in $R(a)$ for both the S1 and S2 solutions are comparable within the error of the model fits (± 0.08 nm). Last, the S2 particles have aspect ratios with larger scatter and a smaller net increase than those of the S1 particles (Figure S7 of the Supporting Information).

Figure 10 summarizes the changes in S2 nanoparticle composition at 70 °C as obtained from absolute intensity analyses of SAXS patterns. S2 particles have lower number

TABLE 2: Net Increase in the Nanoparticle Core Radii for S1 and S2 Solutions^a

T (°C)	S1 solution		S2 solution	
	$\Delta R(a)$ (nm)	$\Delta R(b)$ (nm)	$\Delta R(a)$ (nm)	$\Delta R(b)$ (nm)
70	0.54	0.50	0.34	0.66
80	0.46	0.70	0.37	1.17
90	0.75	1.19	0.65	1.69

^a The values listed in the table are calculated from the differences between the initial and final quantities for solutions over a 320-min period. The $R(a)$ and $R(b)$ values were obtained from model fits to SAXS patterns with an accuracy of ± 0.08 nm.

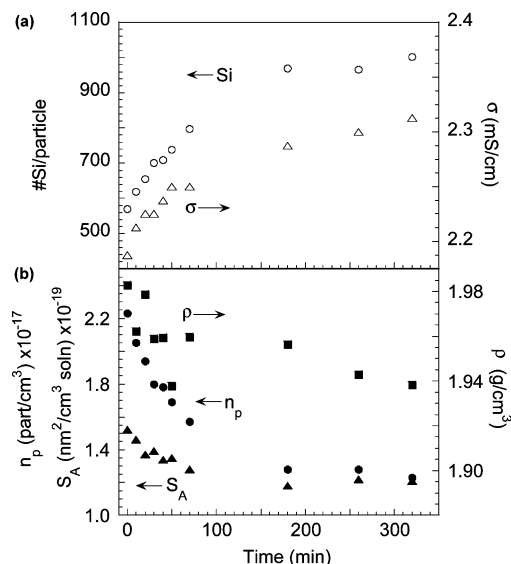


Figure 10. Compositional changes to an S2 solution heated at 70 °C over a 320-min period. (a) Plots of the number of silicon atoms per particle and the experimental conductivity, σ . (b) Plots of the number density, n_p , particle density, ρ , the total surface area of particle cores per volume of solution, S_A .

densities and contain more silicon atoms than the particles formed in the higher-alkaline S1 solutions. The S2 particle density is slightly lower than that of the S1 particle, but the difference is small enough to suggest that the core density is not a strong function of pH within the H₂O/OH range studied.

Analyses of the internal composition of S2 particles were performed analogously to the procedure followed for S1 particles. As shown in Figure 10, the core density decreases during the 320-min period of heating, resulting in a maximum of $63 \pm 8 \times 10^{17}$ TPA/cm³ inclusion in the particle core based on eq 23. Over the course of heating, there is a 20% reduction in the total surface area, which results in a loss of $38 \pm 5 \times 10^{17}$ TPA/cm³ from the surface using eq 21. Thus, the disparity in numbers suggests that TPA inclusion in the S2 particles is not the sole contribution to the change in core density and that perhaps the nanoparticles become more hydrated when heated. However, analyses of the conductivity measurements, shown in Figure 10, reveal that a fraction of displaced TPA is incorporated into the evolved S2 particle core (Figure S8 of the Supporting Information shows the change in conductivity observed experimentally compared to the predicted values using eq 24 for TPA loss from the surface and inclusion into the core).

If we compare the predicted number densities of TPA inclusion for S1 ($45 \pm 6 \times 10^{17}$ TPA/cm³) and S2 ($38 \pm 5 \times 10^{17}$ TPA/cm³) particles, the values are approximately the same—a result that is counterintuitive, considering that the S2 particles are larger in size and have increased surface area for TPA adsorption. The majority of surface area for the oblate

ellipsoid lies along the surface normal to the a axis, and as we have previously shown, the radial growth along the a axis is similar for S1 and S2 particles. Thus, it is possible that TPA coverage varies with solution alkalinity, which would suggest differences in the charge and/or structure of the S1 and S2 nanoparticle surfaces. However, the exact nature of these changes cannot be determined from the results presented in this study.

To summarize the effects of solution pH on nanoparticle evolution, we find that nanoparticles formed at lower pH (S2 solutions) are larger in size and exhibit larger growth along the b axis, while the aspect ratio increases less over time. The number density of particles is reduced, whereas the number of silicon atoms per particle increases; however, the core density, although slightly lower, does not change significantly. Last, we find that the TPA inclusion in the growing nanoparticle core is similar for both S1 and S2 particles, but the latter may become more hydrated during the course of evolution.

Nanoparticle Density. Given the large surface-area-to-volume ratio of the nanoparticles, defining an accurate particle density is a difficult task. The inclusion or removal of surface silanol groups can have a large effect on the density calculation. To more systematically study this affect, the density variation of zeolite ZSM-11 (MEL) was performed. MEL zeolite has a similar density to silicalite-1 with surface silanol groups that lie in the plane of the unit cell, which makes the removal of surface Si–O bonds simpler. Combining 8 MEL unit cells gives a particle with dimensions $4.01 \times 4.01 \times 2.68 \text{ nm}^3$ (volume of 43.2 nm^3) comprising 760 Si atoms—the size and composition of which is similar to the S1 and S2 nanoparticle cores. The particle density is 1.77 g/cm^3 ; however, the removal of surface oxygen (i.e., reducing the volume to 37.4 nm^3) results in an increased density of 2.05 g/cm^3 . Thus, the inclusion of one layer of oxygen generates a significant change in the density of the particle for the size range of the silica nanoparticles.

Fedeyko et al. obtained a density of $1.7 \pm 0.1 \text{ g/cm}^3$ by performing a density gradient analysis on S1 particles ($25 \text{ }^\circ\text{C}$) that were isolated, calcined, and redispersed in solution.¹⁹ From Figures 4 and 10, the particle density obtained from SAXS measurements ranges from 1.94 to 2.01 g/cm^3 , which is substantially higher than the previously reported value. Considering that X-rays primarily scatter from silicon atoms, the ellipsoid radii obtained from SAXS measurements do not account for the Si–O bond length ($\sim 0.12 \text{ nm}$) on the surface of the nanoparticles. Assuming a silanol density of 4.16 sites/nm^2 (estimated from MFI⁴²), the inclusion of the Si–O bond on the surface of the S1 particle reduces the density to $\sim 1.5 \text{ g/cm}^3$. Thus, the observed high density from the SAXS absolute intensity analysis is possibly an artifact related to the sensitivity of the density to the definition of the interface between the particle core and shell.

Nanoparticle Aggregation. Previous studies by de Moor et al. used SAXS to investigate the growth of silicalite-1 from synthesis mixtures containing silicic acid powder of the composition $x \text{ Na}_2\text{O}/1.22 \text{ (TPA)}_2\text{O}/10 \text{ SiO}_2/117 \text{ H}_2\text{O}$ with $x = 0.43\text{--}0.85$.^{23,43} Solutions synthesized from silica powder form a gel network that must first be boiled for $\sim 10 \text{ min}$ to generate a clear solution of nanoparticles. Room-temperature samples of these solutions were measured by de Moor et al., from which they reported nanoparticles with a size of $\sim 2.8 \text{ nm}$ in diameter. Upon heating the solution to $125 \text{ }^\circ\text{C}$, a fraction of the nanoparticles was found to aggregate and form a second population having a size of $\sim 10 \text{ nm}$. The concentration of aggregates was found to be dependent on alkalinity, and aggregation was not observed at high alkalinity ($\text{Si}/\text{OH} = 2.12$).^{23,44}

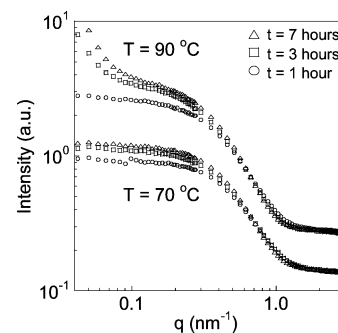


Figure 11. SANS patterns for d-S2 solutions heated at 70 and 90 $^\circ\text{C}$ for 1, 3, and 7 h. Large aggregates are observed at higher temperatures ($T > 70 \text{ }^\circ\text{C}$) after a period of heating the solutions.

Nanoparticle aggregates have also been observed for the solutions in this study. Figure 11 shows SANS scattering patterns for d-S2 solutions heated at 70 and 90 $^\circ\text{C}$. At 70 $^\circ\text{C}$, there are no aggregates or larger particles observed over a 7-h period. For the nanoparticles heated at 90 $^\circ\text{C}$, aggregates are present but do not form until after 1 h of heating. For the d-S1 solution, aggregates do not form at 70 $^\circ\text{C}$ over a 7-h period, but are observed after 3 h at 80 $^\circ\text{C}$ and before 1 h at 90 $^\circ\text{C}$. Therefore, it is observed that nanoparticle aggregation is an activated process. Because of the large length scale of the aggregates, their presence in solution cannot be detected by our SAXS instrument, which can only reach a minimum q value of 0.1 nm^{-1} . Therefore, the aggregates are not observed in SAXS patterns of S1 and S2 solutions.

Nanoparticle solutions were filtered with a $0.45\text{-}\mu\text{m}$ membrane prior to analysis; thus, particle aggregates observed in this study are within 200–450 nm in size, which is nearly an order of magnitude larger than those reported by de Moor et al. The q range required to analyze the aggregate size and shape is outside the range of both SAXS and SANS and would require the use of ultra small-angle neutron scattering (USANS). Until these measurements are conducted, we cannot comment on the exact structure and concentration of these aggregates, nor can we determine if the aggregate size changes as a function of time and temperature.⁴⁵

Summary and Conclusions

The time-dependent evolution of silica–TPA nanoparticles at higher temperatures was studied by small-angle X-ray and neutron scattering to determine the changes in particle size, morphology, and structure. It was found that nanoparticle growth is an irreversible process that occurs via an Ostwald ripening mechanism and is accompanied by the net increase in solution pH and conductivity. The evolved particles retain a core–shell structure, but the particles become more spherical-like, especially at higher values of pH. Furthermore, the composition of the nanoparticle core changes during the evolution to include TPA and possibly water into the core, thereby reducing the overall density of the particle and becoming more zeolite-like. This process is activated with the rate-determining step being a growth rather than a dissolution path and explains the metastable nature of nanoparticles at room temperature whose size and structure presumably evolve extremely slowly. The results obtained from these accelerated evolution studies present a clearer molecular-level understanding of nanoparticle evolution at higher temperatures (those characteristic of zeolite growth) and thus establish the groundwork toward future analysis of silicalite-1 nucleation and growth.

Acknowledgment. This work was funded in part by the National Science Foundation Nanoscale Interdisciplinary Research Team (NIRT) under grant 0103010. We acknowledge the support of the National Institute of Standards and Technology, U.S. Department of Commerce, in providing the neutron research facilities used in this work. We thank B. Hammouda, D. Ho, and S. Kline for discussions and assistance with the SANS experiments, Joe Fedeyko and Amit Kumar for help with collecting SANS data, and H. Schnablegger (Anton Paar GmbH, Graz/Austria) for discussion of SAXS analysis.

Supporting Information Available: Tables containing scattering length densities, error analysis of absolute intensity calculations, and comparisons of the S1 and S2 particle shell thickness. Figures containing Guinier, dimerization, and polydispersity analyses along with fits to experimental SAXS and conductivity data. The results of the S2 solution analyses are provided (conductivity calculations, particle aspect ratios, and core-shell structure verification). This material is available free of charge via the Internet at <http://pubs.acs.org>.

References and Notes

- Nicolakis, V.; Kokkoli, E.; Tirrell, M.; Tsapatsis, M.; Vlachos, D. G. *Chem. Mater.* **2000**, *12*, 845.
- Watson, J. N.; Iton, L. E.; Keir, R. I.; Thomas, J. C.; Dowling, T. L.; White, J. W. *J. Phys. Chem. B* **1997**, *101*, 10094.
- Schoeman, B. J.; Sterte, J.; Otterstedt, J. E. *Zeolites* **1994**, *14*, 568.
- Yang, S. Y.; Navrotsky, A. *Chem. Mater.* **2002**, *14*, 2803.
- Rimer, J. D.; Kragten, D. D.; Tsapatsis, M.; Lobo, R.; Vlachos, D. *14th International Zeolite Conference Proceedings*; Cape Town, South Africa, 2004; p 317.
- Kirschhock, C. E. A.; Ravishankar, R.; Jacobs, P. A.; Martens, J. A. *J. Phys. Chem. B* **1999**, *103*, 11021.
- Schoeman, B. J. *Microporous Mesoporous Mater.* **1998**, *22*, 9.
- Fedeyko, J. M.; Vlachos, D. G.; Lobo, R. F. *Langmuir* **2005**, *21*, 5197–5206.
- Mann, S. *Nature (London)* **1988**, *332*, 119.
- Vrieling, E. G.; Beelen, T. P. M.; van Santen, R. A.; Gieskes, W. W. C. *J. Biotechnol.* **1999**, *70*, 39.
- Mann, S.; Burkett, S. L.; Davis, S. A.; Fowler, C. E.; Mendelson, N. H.; Sims, S. D.; Walsh, D.; Whilton, N. T. *Chem. Mater.* **1997**, *9*, 2300.
- Lai, Z.; Bonilla, G.; Diaz, I.; Nery, J. G.; Sujaoti, K.; Amat, M. A.; Kokkoli, E.; Terasaki, O.; Thompson, R. W.; Tsapatsis, M.; Vlachos, D. G. *Science* **2003**, *300*, 456.
- Schoeman, B. J. *Microporous Mater.* **1997**, *9*, 267.
- Ravishankar, R.; Kirschhock, C. E. A.; Knops-Gerrits, P.-P.; Feijen, E. J. P.; Grobet, P. J.; Vanoppen, P.; De Schryver, F. C.; Miehe, G.; Fuess, H.; Schoeman, B. J.; Jacobs, P. A.; Martens, J. A. *J. Phys. Chem. B* **1999**, *103*, 4960.
- Ravishankar, R.; Kirschhock, C.; Schoeman, B. J.; De Vos, D.; Grobet, P. J.; Martens, J. A. *12th International Zeolite Conference*, Baltimore, MD, July 1998; Treacy, M. M. J., Marcus, B. K., Bisher, M. E., Higgins, J. B., Eds.; MRS Publications: 1999, p. 1825.
- Ravishankar, R.; Kirschhock, C. E. A.; Knops-Gerrits, P.-P.; Feijen, E. J. P.; Grobet, P. J.; Vanoppen, P.; De Schryver, F. C.; Miehe, G.; Fuess, H.; Schoeman, B. J.; Jacobs, P. A.; Martens, J. A. *J. Phys. Chem. B* **1998**, *102*, 2633.
- Kragten, D. D.; Fedeyko, J. M.; Sawant, K. R.; Rimer, J. D.; Vlachos, D. G.; Lobo, R. F.; Tsapatsis, M. *J. Phys. Chem. B* **2003**, *107*, 10006.
- Schoeman, B. J.; Regev, O. *Zeolites* **1996**, *17*, 447.
- Fedeyko, J. M.; Rimer, J. D.; Lobo, R. F.; Vlachos, D. G. *J. Phys. Chem. B* **2004**, *108*, 12271.
- de Moor, P. P. E. A.; Beelen, T. P. M.; Komanshek, B. U.; Beck, L. W.; Wagner, P.; Davis, M. E.; van Santen, R. A. *Chem.—Eur. J.* **1999**, *5*, 2083.
- Yang, S. Y.; Navrotsky, A.; Wesolowski, D. J.; Pople, J. A. *Chem. Mater.* **2004**, *16*, 210.
- Kirschhock, C. E. A.; Kremer, S. P. B.; Grobet, P. J.; Jacobs, P. A.; Martens, J. A. *J. Phys. Chem. B* **2002**, *106*, 4897.
- de Moor, P.-P. E. A.; Beelen, T. P. M.; van Santen, R. A.; Beck, L. W.; Davis, M. E. *J. Phys. Chem. B* **2000**, *104*, 7600.
- de Moor, P. P. E. A.; Beelen, T. P. M.; van Santen, R. A.; Tsuji, K.; Davis, M. E. *Chem. Mater.* **1999**, *11*, 36.
- Lindner, P.; Zemb, T. *Neutrons, X-rays, and light: scattering methods applied to soft condensed matter*, 1st ed.; North-Holland Delta Series; Elsevier: Amsterdam, 2002.
- Glatter, O. *J. Appl. Crystallogr.* **1977**, *10*, 415.
- Glatter, O. *J. Appl. Crystallogr.* **1980**, *13*, 577.
- Pedersen, J. S. *Adv. Colloid Interface Sci.* **1997**, *70*, 171.
- NIST SANS Analysis Package, freely available at www.ncnr.nist.gov/programs/sans/manuals/data_anal.html.
- Feigin, L. A.; Svergun, D. I. *Structure Analysis by Small-Angle X-ray and Neutron Scattering*; Taylor, G. W., Ed.; Plenum Press: New York, 1987.
- Guinier, A.; Fournet, G. *Small-Angle Scattering of X-rays*; Wiley: New York, 1955.
- Petit, J. M.; Law, B. M.; Beysens, D. *J. Colloid Interface Sci.* **1998**, *202*, 441.
- Orthaber, D.; Bergmann, A.; Glatter, O. *J. Appl. Crystallogr.* **2000**, *33*, 218.
- Cundy, C. S.; Forrest, J. O.; Plaisted, R. J. *Microporous Mesoporous Mater.* **2003**, *66*, 143.
- Glatter, O. *J. Appl. Crystallogr.* **1979**, *12*, 166.
- Claesson, P.; Horn, R. G.; Pashley, R. M. *J. Colloid Interface Sci.* **1984**, *100*, 250.
- Calculations of TPA in Si-ZSM-5 are made using the densities for the zeolite with and without occluded TPA, which are taken as 2.03 and 1.80 g/cm³, respectively.
- Hibbert, D. B.; James, A. M.; Davies, C. W. *Dictionary of Electrochemistry*. 2nd ed.; Wiley: New York, 1984.
- Atkins, P. W. *Physical Chemistry*; Freeman: New York, 1998.
- Castellan, G. W. *Physical Chemistry*, 3rd ed.; Addison-Wesley: Reading, MA, 1983.
- Watson, J. N.; Iton, L. E.; White, J. W. *Chem. Commun.* **1996**, 2767.
- Nicolakis, V.; Tsapatsis, M.; Vlachos, D. G. *Langmuir* **2003**, *19*, 4619.
- de Moor, P.-P. E. A.; Beelen, T. P. M.; Komanshek, B. U.; Diat, O.; van Santen, R. A. *J. Phys. Chem. B* **1997**, *101*, 11077.
- de Moor, P.; Beelen, T. P. M.; van Santen, R. A. *J. Phys. Chem. B* **1999**, *103*, 1639.
- Guinier plots were generated from SANS patterns of all d-S1 and d-S2 samples to ascertain whether the presence of aggregates would affect the fitting of the scattering patterns (analysis of the d-S2 solution at 90 °C is shown in Figure S9 of the Supporting Information). From the analyses of the scattering patterns, a deviation from linearity for ellipsoids falls within the range 0.03 < q^2 < 0.08 (nm⁻²). Therefore, all SANS and SAXS patterns in this study were analyzed at $q > 0.2$ nm⁻¹.